MEASUREMENT OF FLOW FIELD NEAR A TIP LEAKAGE VORTEX CAVITATION IN A TURBOPUMP INDUCER

J. Kim

Doosan Heavy Industry

S. Jin Song

Seoul National University

Keywords: turbopump inducer, tip leakage vortex, cavitation

ABSTRACT

Flow field near the tip region of a turbopump inducer has been measured using Particle Image Velocimetry (PIV) method in a cavitating condition. Tip leakage vortex cavitation in an inducer leads to hydraulic instabilities, thus, the effects of tip leakage vortex cavitation on a flow field near the blade need to be investigated. Using the tilted laser sheet, flow field near the tip leakage vortex cavitation has been measured. Two different sizes of tip leakage vortex cavitation has been compared. For a small cavitation region, the flow field near the inducer blade is not affected by tip leakage vortex cavitation. Thus, an incidence angle near the leading edge of the inducer blade is positive. On the other hand, for a large cavitation region, tip leakage vortex cavitation increases the axial and absolute tangential velocity near the leading edge of the inducer blade. Thus, the incidence angle becomes negative. Such measurements give clues to understand the mechanism of hydraulic instabilities induced by tip leakage vortex cavitation.

NOMENCLATURE

D	inducer diameter
p_v	vapor pressure
r	inducer radius
u	Velocity vector
V_a	Axial velocity
V_t	Tangential velocity at the tip
$V_{t,rel}$	Relative tangential velocity at the tip
ρ	liquid density
α_{1t}	Incidence angle at blade tip
σ	cavitation number, $= (p_1 - p_v)/\frac{1}{2}\rho r^2 \Omega^2$
β	blade tip angle
Ω	inducer rotational speed, rotational frequency (Hz)

Subscripts

1	inlet
2	outlet

INTRODUCTION

To achieve high performance and reliable control of thrust, liquid propellants are mostly used to rocket engine system recently. For liquid rocket engines, turbopumps supply liquid oxidizer and fuel to the combustion chamber at high pressure. To reduce the size and weight of the entire rocket engine, turbopumps rotate at high speeds under low pressure oxidizer and propellant. Such requirements lead to cavitation in turbopumps. Therefore, to inhibit cavitation in the impeller, an axial type inducer with a long flow path is installed upstream of a turbopump. However, the inducer itself also can suffer from cavitation. Turbopump inducer cavitation can cause hydraulic instabilities, or cavitation instabilities, including rotating cavitation, asymmetric attached cavitation, and cavitation surge [1, 2].

Initially, the analysis of cavitation instabilities had been conducted by considering cavitation regions as 2-D attached cavitation, which occurs in hydrofoil or cascade. Watanabe et al [3]. and Horiguchi et al [4]. developed an analytical model to predict the criterion for cavitation instability in 2-D cascade using singularity and closed cavity model. They proposed that the cavitation instability occurs when the cavitation length is 65 % of the blade pitch length and validated with the experimental results. However, other experimental results [5] showed different results with which the criterion does not agree. Iga et al. [6, 7] simulated cavitation instabilities in 2-D cascade. The propagation speed mechanism of rotating instability was proposed based on the natural characteristics of the break-off frequency of attached cavitation.

However, these 2-D cascade model and simulations could not be applied to the real inducer where the tip leakage vortex caviation plays an important role in cavitation instabilities. Kimura et al. [8] measured the flow coefficients where rotating cavitation occurs and simulated non-cavitating 3-D inducer to investigate the tip leakage vortex propagation. They found that the flow coefficient where rotating cavitation occurs corresponds to the flow coefficient at which tip vortex cavitation interacts with the next blade. Hosangadi et al. [9] performed numerical

simulation for 4-blade SSME low pressure fuel pump inducer. They found that the interaction of the cavitation region with neighboring blade leads to rotating cavitation. Kang et al. [10] explained the propagation mechanism of rotating cavitation through 3-D CFD simulation. When cavitation region increases, the incidence angle of next blade is decreased and the cavitation region of the next blade also is also decreased. Therefore, the propagation of rotating cavitation is forward to the inducer rotation. Tani et al. [11] also performed 3-D CFD under rotating cavitation with the different flow rate. They found out that the incidence angle changes near the leading edge of the blade under rotating cavitation due to the cavitation collapse. For the low flow coefficient, the relative incidence angle change is small, thus rotating cavitation did not occur. Lettieri et al. [12] visualized cavitating inducer under rotating cavitation. They found out that the tip leakage vortex cavitation interacting with the following blade leads to rotating cavitation. However, they did not measure the flow field to explain the mechanism.

Until now, numerical simulations for rotating cavitation have been performed by unsteady Reynolds Averaged Navier Stokes (RANS). However, simulations with RANS cannot predict tip leakage vortex cavitation accurately. Therefore, this study aims to measure the velocity field near the leading edge of the inducer tip region to understand tip leakage vortex cavitation effects using Particle Image Velocimetry (PIV) method.
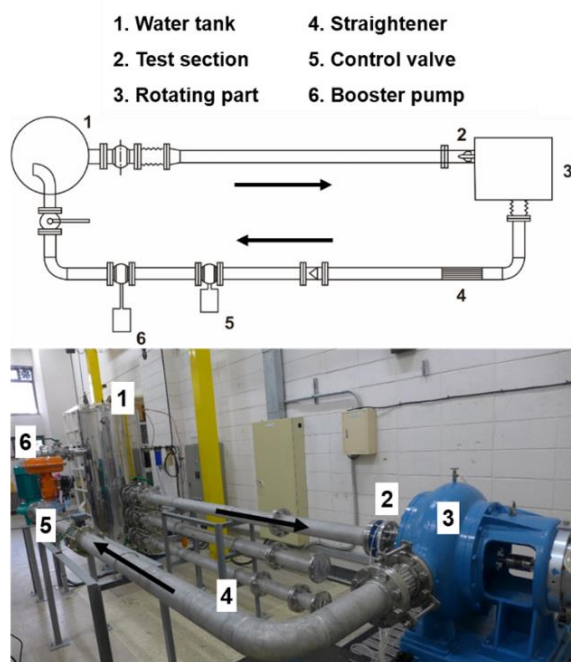
TEST FACILITY

The closed-loop turbopump inducer test facility at Seoul National University depicted in Fig. 1 has been used. The test facility is described in detail in Kim and Song [13], and only a brief summary is given here. It consists of a water tank, an inducer, a motor, a straightener, a flow meter, a control valve, a vacuum pump, and a booster pump. The maximum power and rotational speed of the motor are 60-kW and 10,000 rpm, respectively. The rotational speed is adjusted by a variable frequency-drive within ±1 rpm. The pressure in the test facility is adjusted with a vacuum pump and compressed air in the water tank. Using a booster pump and control valve, the flow coefficient has been fixed at the designated flow coefficient to within the 0.11 % (less than the uncertainty) during the experiments.

The test inducer provided by the Korea Aerospace Research Institute (KARI) is shown in Fig. 2. The test inducer has 3 blades; its diameter is 0.094 m; and its design flow coefficient is 0.096. Its specifications are summarized in Table. 1 [14].

PIV SET UP

The purpose of this study is to measure the flow field, including incidence angle, near the tip region under rotating cavitation condition. The incidence angle, α, is defined as follows.

$$\alpha = \beta_{1t} - \tan^{-1} \frac{V_a}{V_{t,rel}} \qquad (1)$$

Table 1: Design characteristics of the test inducer.

Parameters		Value
Diameter (D)		0.094 m
Design flow coefficient (ϕ_d)		0.096
Blade number		3
Solidity at tip		2.7
Blade tip angle	Inlet (β_{1t})	9.6 deg
	Outlet (β_{2t})	15.0 deg

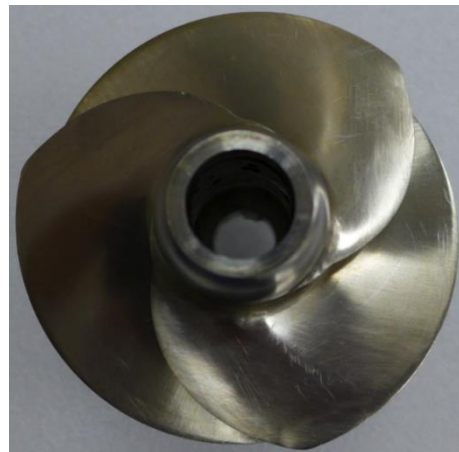Figure 1: SNU turbopump inducer experimental facilicy
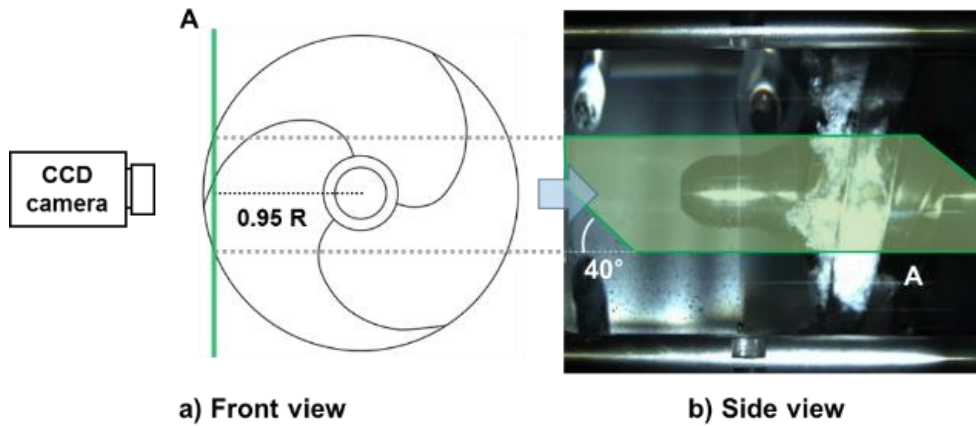

Figure 2: Test inducer

66

Figure 3: PIV measurement location

Figure 3 shows the PIV measurement plane. Laser sheet has been aligned at the 0.95 radius of the inducer (Fig. 3 (a)) to simultaneously measure the axial and tangential velocities. When the laser sheet is aligned correctly, the region in Fig. 3 (b) is brightened.

PIV measurement system is composed of a light source, image recorder (CCD camera), light sheet optics, and synchronizer as depicted in Fig. 4. The double-cavity Q-switched Nd:YAG Laser (New Wave Solo) has been used. To make a thin laser
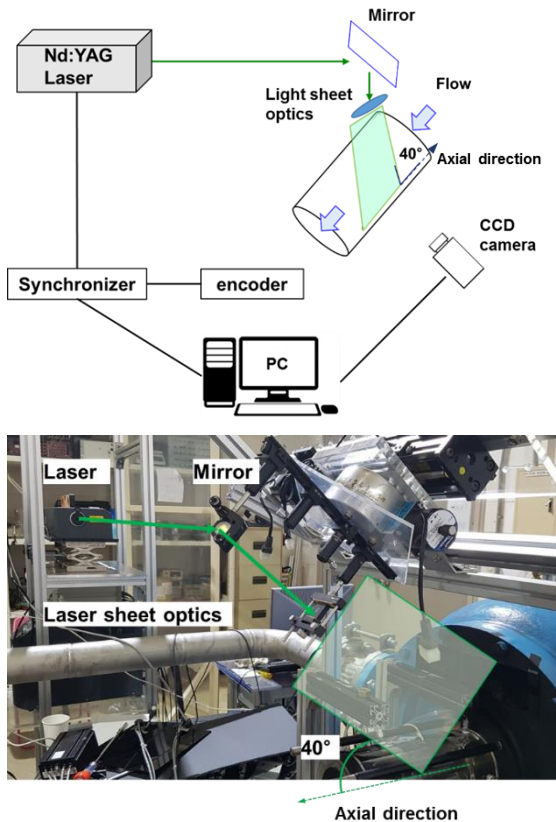

Figure 4: PIV measurement system

Table 2: Specification of PIV measurement system.

Laser	New Wave Solo
	ND;Yag-532 nm
	Power: 120 mJ
	Width: 4 mm
Camera	PCO Sensicam, 12 bit
	1376 x 1040 pixels
	Pixel size: 6.45 x 6.45 µm
	Repetition 10 Hz
Synchronizer	Quantum Composers 9518+
	Resolution: 1 ns
	Accuracy: 1 ns + .0001 delay
	Max. frequency: 5 MHz
Seed	Silver coated hollow glass spheres Diameter: 10 µm Stokes number: 0.003

sheet, a 1.2 mm slot has been installed before the laser sheet enters the inducer casing. A CCD camera (PCO Sensicam) with 1376x1040 pixels (pixel size: 6.45 µm x 6.45 µm) has been used to record images. Focal length and f-number of the camera lens (Nikon) used in this study are 45 mm and 4, respectively. A synchronizer (Quantum composers 9518+ pulse generator) with 8 independent signal output channels has been used as the trigger signal. Resolution and accuracy are 1 ns and 1 ns + .0001 delay, respectively. The signal is triggered by the encoder signal from the motor; thus, the PIV images have been obtained at a fixed tangential orientation of the inducer. In the present study, silver coated hollow glass spheres with a 10 µm diameter (which are neutrally buoyant) have

been selected as the tracer particle. Small cavitation bubbles also act as tracer particles. Specifications of the PIV system are summarized in Table 2.

Previously, PIV measurement had been performed in a turbopump inducer to investigate the flow field upstream of the inducer [15]. The laser sheet was aligned with the axis of the inducer. However, in this study, PIV measurement has been performed in cavitating condition to capture the flow field near the tip region of the inducer blade. To stratify the objectives, the designs of laser sheet direction and calibration target is carefully considered.

When laser sheet is aligned in the vertical direction, the cavitation region blocks the laser sheet, thus, the velocity field beneath the cavitation region cannot be evaluated. To avoid the blocking effects of cavitation region, the laser sheet has been tilted by 40° relative to the axial direction (Figs. 3 (b) and 4).

PIV measurement has been performed in water. Therefore, it is required to calibrate in water. It is difficult to place the calibration target at the tip region exactly. A movable L-shaped acrylic calibration target (34.76 mm × 80 mm) has been manufactured. When the target contacts with the inducer casing, it is placed at the radial location corresponding to the 95 % of the span of the inducer blade (Fig. 5 (a)). 2 mm × 2 mm grids have been engraved on the calibration plate. Experiments are performed in transparent casing, thus, it is possible to have the distortion effects in vertical direction. Using the calibration picture as shown in Fig. 5 (b), the number of pixels in the vertical direction of each grid needs to be measured to compensate for the distortion effects. The measured number of pixels for each grid in the vertical direction are the same at 43 pixel ± 1 pixel. Therefore, the distortion effects caused by the casing can be ignored.

The velocity vector fields from the PIV measurement has been evaluated with the commercial PIV software DynamicStudio 6 from Dantec. The time interval has been set at 20 μs, during which the particle moves about 4-8 pixels. In this study, the velocity gradient is high near the rotating inducer blade, and conventional PIV data processing methods is not suitable. Therefore, an 'adaptive PIV' algorithm, which facilitates more accurate results in the high velocity gradient flows, has been used [16]. The interrogation areas of 32x32 pixels with a 50 % overlap have been used, resulting in 5,440 vectors for the 1,360 x 1,040 pixels. The ratio of error vector is less than 2.5 %, and the final results have then been smoothed once with a 3x3 Gaussian kernel. Peak validation has been performed with the minimum accepted 0.25 peak height, 1.15 peak height ratio, and 4.0 S/N ratio. Figure 8 shows a raw PIV image of tracer particles under a cavitating condition.
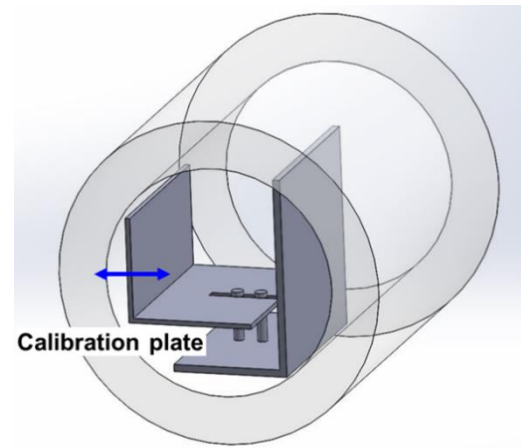
(a) Calibration target plate
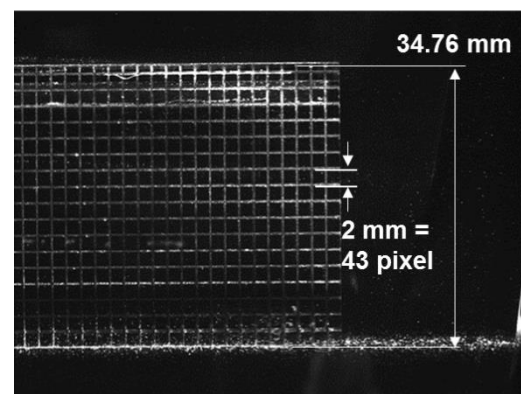
(b) Calibration picture

Figure 5: Calibration target plate (a) and calibration target picture with laser sheet (b)
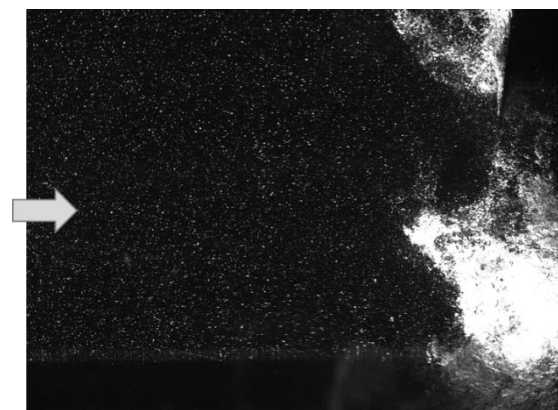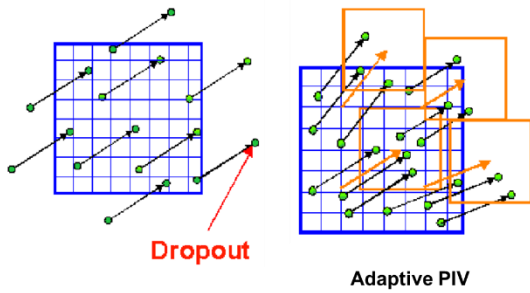

Figure 6: Raw image of tracer particles
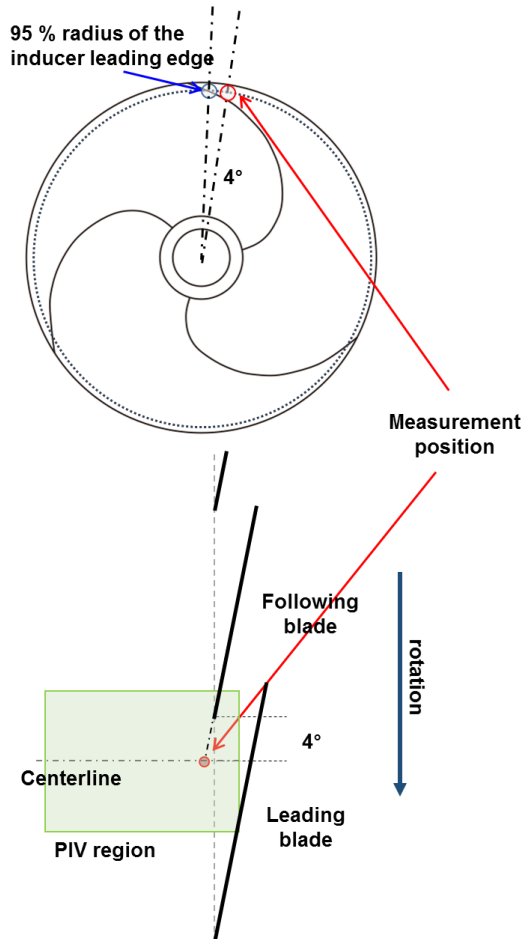
Figure 7: Principle of Adaptive PIV method [16]

Figure 8: PIV region and incidence angle measurement point
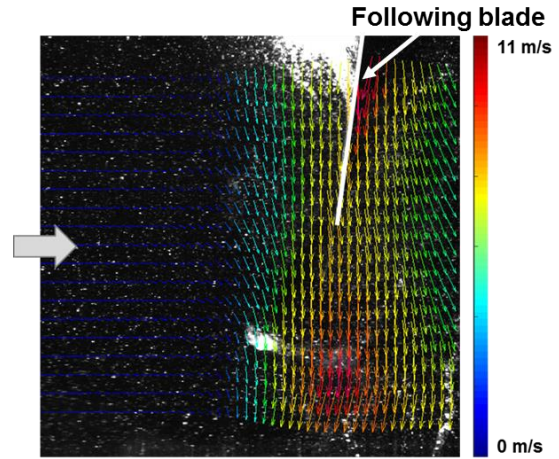

Figure 9: Raw image and velocity vector (50 frames phase-locked ensemble averaged) in case of the small cavitation region
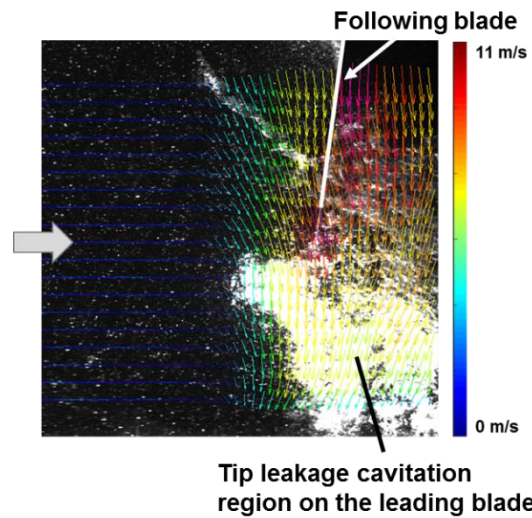

Figure 10: Raw image and velocity vector (24 frames phase-locked ensemble average) in case of the large cavitation region

RESULTS AND DISCUSSION

Figure 8: shows PIV measurement region and incidence angle measurement position. PIV measurement region (green area) includes the leading edge of the following blade. Thus, flow field change near the leading edge of the following blade due to the tip leakage vortex cavitation region on the leading blade can be evaluated. The incidence angle near the inducer leading edge at 95 % radius has been measured at an azimuthal location 4° ahead of the leading edge along the blade angle direction [17].

The inducer flow is 3-D flow, thus, the velocity component perpendicular to the light sheet cannot be measured by 2-D PIV measurement. Therefore. the incidence angle is accurate only on the centerline. To obtain the exact incidence angle, the PIV images have been obtained when the measurement point of the incidence angle is located on the center line of the image (Fig. 8) for the accurate incidence angle measurement. Elsewhere, to compensate for the 3-D flowthe measured velocity has been corrected by the projection method to compensate for the 3-D flow.

PIV images near the tip region of the inducer blade have been obtained under cavitating condition. At $\sigma=0.070$, cavitation region at inducer blade becomes uneven forming small and large cavitation region as reported in Kim and Song [18]. Small and large tip leakage vortex cavitation regions have been compared, and 50 and 24 PIV images of similar tip leakage vortex cavitation

69

regions have been phase-locked ensemble averaged, respectively.

Figure 9 shows a raw image with absolute

tip leakage vortex cavitation region on the leading blade can be a clue to understand the mechanism of rotating cavitation.
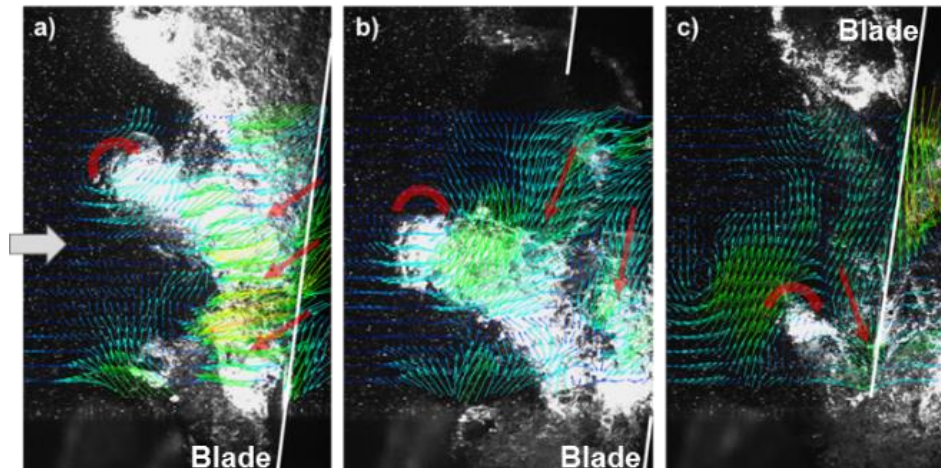

Figure 11: Velocity vectors of rotating cavitation conditions is subtracted from non-cavitating velocity vectors with different position of blade and tip leakage vortex cavitation region

velocity vectors when the cavitation region on the leading blade is small. Tip leakage vortex cavitation on the leading blade cannot be seen at the bottom of the picture because the cavitation region on the leading blade is not sufficiently large. Flow comes from left to right, and the absolute tangential velocity increases as the flow approaches the inducer blade due to the inducer rotation. Incidence angle at the leading edge of the following blade is positive at 6.7° (ranging from 4.3° to 9.4°).

Figure 10 shows a raw image with absolute velocity vectors when the cavitation region on the leading blade is large. The tip leakage vortex cavitation region on the leading blade is large enough to reach the leading edge of the following blade. Axial and absolute tangential velocities near the leading edge of the following blade are higher than the small tip leakage vortex cavitation case. The closure region of the tip leakage vortex cavitation increases axial and absolute tangential velocities. Thus, the incidence angle at the leading edge of the following blade becomes negative at -4.4° (ranging from -1.9° to -8.3°).

Figure 11 shows the velocity vectors of cavitating condition subtracted from non-cavitating velocity vectors (σ=1.12) with different position of blade and tip leakage vortex cavitation region. The velocity vector subtraction is not an accurate method, but it can approximately give clues how tip leakage vortex cavitation affects the flow field. White bar represents the blade. There are vortex core near the closure region of the tip leakage vortex cavitation region (red circular arrows) and penetration flow downward (red arrows heading to downward). Tip leakage vortex cavitation changes the flow field of the following blade.

At σ=0.070, rotating cavitation is occurred as reported in Kim and Song [18]. The changes in incidence angle of the following blade due to the

REFERENCES

[1] Ryan, R. S.; 1994. "The Space Shuttle Main Engine Liquid Oxygen Pump High-Synchronous Vibration Issue, the Problem, the Resolution Approach, the Solution," 30th Joint Propulsion Conference and Exhibit, AIAA Paper 1994-3153.

[2] Tsujimoto, Y.; Yoshida, Y.; Maekawa, Y.; Watanabe, S. and Hashimoto, T.; 1997. "Observations of Oscillating Cavitation of an Inducer," Journal of Fluids Engineering, Vol. 119, pp. 775-781.

[3] Watanabe, S.; Sato, K.; Tsujimoto, Y.; Kamijo, K.; 1999. "Analysis of Rotating Cavitation in a Finite Pitch Cascade Using a Closed Cavity Model and a Singularity Method," Journal of Fluids Engineering, Vol. 121, pp. 834-840.

[4] Horiguchi, H.; Watanabe, S.; Tsujimoto, Y.; 2000. "A Linear Stability Analysis of Cavitation in a Finite Blade Count Impeller," Journal of Fluids Engineering, Vol. 122, No. 4, pp. 798-805.

[5] Franc. J. P.; Boitel, G.; Riondet, M.; Jason, E.; Ramina, P. and Rebattet, C.; 2010. "Thermodynamic Effect on a Cavitating Inducer-Part 1: Geometrical Similarity of Leading Edge Cavities and Cavitation Instabilities," Journal of Fluids Engineering, Vol. 132, p. 021303.

[6] Iga, Y.; Nohml, M.; Goto, A.; Shin, B. R. and Ikohagi, T.. "Numerical Study of Sheet Cavitation Breakoff Phenomenon on a Cascade Hydrofoil," Journal of Fluids Engineering, Vol. 125, pp. 643-651.

[7] Iga, Y.; Nohml, M.; Goto, A.; Ikohagi, T.; 2004. "Numerical Analysis of Cavitation Instabilities Arising in the Three-Blade Cascade," Journal of Fluids Engineering, Vol. 126, pp. 419-429.

[8] Kimura, T.; Yoshida, Y.; Hashimoto, T.; Shimagaki, M.; 2008. "Numerical Simulation for Vortex Structure in a Turbopump Inducer: Close Relationship with Appearance of Cavitation Instabilities," Journal of Fluids Engineering, Vol. 130, p. 051104.

[9] Hosangadi, A.; Ahuja, V. and Ungewitter, R. J.; 2007. "Simulations of Rotational Cavitation Instabilities in the SSME LPFT Inducer," 43rd AIAA/ASME/SAE/ASEE Joint Propulsion Conference & Exhibit, Cincinnati, OH, Report No. AIAA 2007-5536.

[10] Kang, D.; Yonezawa, K.; Horiguchi, H.; Kawata, Y.; Tsujimoto, Y.; 2009. "Cause of cavitation instabilities in three dimensional inducer," International Journal of Fluid Machinery and Systems, Vol. 2 (3), pp. 206-214.

[11] Tani, N.; Yamanishi, N.; Tsujimoto, Y.; 2012. "Influence of Flow Coefficient and Flow Structure on Rotational Cavitation in Inducer," Journal of Fluids Engineering, Vol. 134, p. 021302.

[12] Lettieri, C.; Spakovszky, Z.; Jackson, D. & Schwille, J.; 2017. "Characterization of Cavitation Instabilities in a Four-Bladed Turbopump Inducer," Journal of Propulsion and Power.

[13] Kim, J. and Song, S. J.; 2016. "Measurement of temperature effects on cavitation in a turbopump inducer." Journal of Fluids Engineering, Vol. 138, p. 011304.

[14] Choi, C.; Noh, J.; Kim, J.; Hong, S. and Kim, J.: 2006. "Effects of a Bearing Strut on the Performance of a Turbopump Inducer," Journal of Propulsion and Power, pp. 1413-1417.

[15] Shimagaki, M.; Watanabe, M.; Hashimoto, T.; Hasegawa, S.; Yoshida, Y. and Nakamura, N.; 2006. "Effect of the casing configurations on the internal flow in rocket pump inducer." 42nd AIAA/ASME/SAE/ASEE Joint Propulsion Conference & Exhibit, Sacramento, California.

[16] Theunissen, R.; 2010. Adaptive image interrogation for PIV: application to compressible flows and interfaces, PhD Thesis, TU Delft, Delft University of Technology.

[17] Tani, N.; Yamanishi, N.; Tsujimoto, Y.; 2012. "Influence of Flow Coefficient and Flow Structure on Rotational Cavitation in Inducer," Journal of Fluids Engineering, Vol. 134, p. 021302.

[18] Kim, J. and Song, S. J.; 2017. "Measurement of thermal parameter and Reynolds number effects on cavitation instability onset in a turbopump inducer," Journal of Global Power and Propulsion Society, Vol. 1, #H5DYU3